Atomic Layer Deposition of Metastable β-Fe$_2$O$_3$ via Isomorphic Epitaxy for Photoassisted Water Oxidation

Jonathan D. Emery,[†] Christian M. Schlepütz,[‡] Peijun Guo,[§] Shannon C. Riha,[†] Robert P. H. Chang,[§] and Alex B. F. Martinson*,[†]

[†]Materials Science Division and [‡]X-ray Science Division, Argonne National Laboratory, 9700 South Cass Avenue, Argonne, Illinois 60439, United States

[§]Department of Materials Science and Engineering, Northwestern University, 2220 Campus Drive, Evanston, Illinois 60208, United States

S Supporting Information

ABSTRACT: We report the growth and photoelectrochemical (PEC) characterization of the uncommon bibyite phase of iron(III) oxide (β-Fe$_2$O$_3$) epitaxially stabilized via atomic layer deposition on an conductive, transparent, and isomorphic template (Sn-doped In$_2$O$_3$). As a photoanode, unoptimized β-Fe$_2$O$_3$ ultrathin films perform similarly to their ubiquitous α-phase (hematite) counterpart, but reveal a more ideal bandgap (1.8 eV), a ~0.1 V improved photocurrent onset potential, and longer wavelength (>600 nm) spectral response. Stable operation under basic water oxidation justifies further exploration of this atypical phase and motivates the investigation of other unexplored metastable phases as new PEC materials.
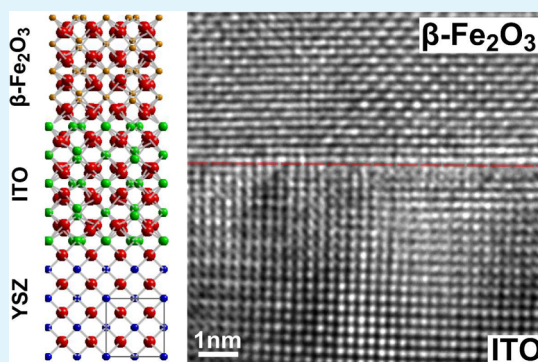
KEYWORDS: atomic layer deposition, iron(III) oxide, α-Fe$_2$O$_3$, β-Fe$_2$O$_3$, PEC water oxidation, epitaxial stabilization

Semiconducting thin films suitable for large-scale solar energy conversion applications are limited to a class of materials that are nontoxic, inexpensive, easily processable, and earth abundant. It is, however, possible to broaden or improve the properties of this narrow class of materials through synthesis and utilization of uncommon, metastable phases. Such stabilized phases can be selected via judicious tuning of, for example, growth conditions, substrate selection, morphology, or postprocessing. Epitaxial phase stabilization is one route used to select a nonequilibrium phase over an equilibrium phase (see reviews 1−3 and references therein). The energetic benefits gained from the formation of a (semi-) coherent, lattice-matched interface during epitaxial growth not only allows for selection of metastable crystalline phases, but also provides an opportunity to improve thin film crystalline quality through larger grain size, more uniform nucleation, and creation of low defect density crystallites and interfaces.[2] This stabilization technique has not only enabled fundamental studies of many rare phases, but in some cases has yielded materials possessing improved properties and new functionality in, for example, fields such as multiferroics,[4] nonlinear optics,[5] and high-temperature superconductors.[6]

Atomic layer deposition (ALD) has become one of the most versatile routes to producing high-quality metal oxides, sulfides, nitrides, and many pure metals.[7−9] ALD is a sequential, self-limiting growth technique that is, by nature, well-suited to conformal, large-area coating of high aspect ratio frameworks with subnanometer digital thickness control. Although not typical, a small subset of ALD processes has been observed to produce epitaxial thin films by utilizing a suitable substrate (see ref 9 and references therein). In this Letter, we report two technologically relevant additions to this epitaxial ALD subset which utilize cubic yttria-stabilized zirconia (YSZ) as the single crystal support. First, we briefly report the epitaxial ALD of Sn-doped In$_2$O$_3$ (ITO) on YSZ. Then, we use this epitaxial ITO/YSZ heterostructure as an isomorphic growth template for the stabilization of the metastable bixbyite phase of iron(III) oxide (β-Fe$_2$O$_3$), enabling a scalable, low-temperature (~200 °C), and highly controlled production method for β-Fe$_2$O$_3$. The uncommon β phase is assessed as a photoanode for the photoassisted oxidation of water and is found to behave comparably to the commonly studied α-Fe$_2$O$_3$ (hematite), but is able to harvest a larger range of the visible spectrum and exhibits a more favorable onset potential as observed in the presence of an efficient hole scavenger.

There are a limited number of earth-abundant materials known to satisfy the demands required of the photoabsorber for practical photoelectrochemical (PEC) water oxidation.[10−13] Some of the most successful are visible-gap semiconductors, which must generate holes with sufficient potential to oxidize

water, and with lifetimes long enough to overcome the sluggish kinetics of the oxygen evolution reaction (OER). The corrosive aqueous operating conditions further reduce the list of viable candidates expected to endure this environment to only a handful of the most robust materials, most of which are oxides. To date, hematite is one of the most promising of these anode materials.[14,15] α-Fe$_2$O$_3$ is a stable phase of iron(III) oxide and exhibits a corundum structure (space group $R\bar{3}c$) with a 1.9−2.2 eV bandgap and valence band sufficiently positive to oxidize water. Within the last 10 years, improvements in control of morphology, doping, and surface chemistry of α-Fe$_2$O$_3$ photoanodes have spurred a series of improved solar-to-hydrogen conversion efficiencies,[14] with record PEC water oxidation photocurrent presently at 4.32 mA/cm^2 at 1.23 V vs the reversible hydrogen electrode (RHE), providing a net solar-to-current efficiency of ∼0.6%.[16]

PEC investigations of non-hematite iron oxide binary phases, including Fe$_{1-x}$O, β-Fe$_2$O$_3$, γ-Fe$_2$O$_3$, ε-Fe$_2$O$_3$, and Fe$_3$O$_4$, are scarce. This is due to various deficiencies including a very small bandgap (Fe$_3$O$_4$ [0.1 eV]), degenerate doping (Fe$_{1-x}$O and Fe$_3$O$_4$), or challenges associated with synthesis as electrodes (β-Fe$_2$O$_3$ and ε-Fe$_2$O$_3$). The β-Fe$_2$O$_3$ polymorph, which is our focus here, has no reported natural occurrence, and possesses a bixbyite-type crystal structure (space group $Ia\bar{3}$) with lattice parameter a = 9.40.[17] It has been synthesized in nanoparticulate form via hydrolysis of FeCl$_3$,[17] solid-state reaction with NaCl and Fe$_2$(SO$_4$)$_3$,[18,19] and thermal decomposition of either Fe(C$_{10}$H$_9$CHO) or FeSO$_4$ in mesoporous SiO$_2$.[20] Thin films of varying purity have also been fabricated using chemical vapor deposition.[21−24] Researchers are now exploring the application of β-Fe$_2$O$_3$ for pigments,[25] sensing,[26,27] and photoreformation of renewable oxygenates.[28]

β-Fe$_2$O$_3$ is thermodynamically unstable, with reports of transformation to either α-Fe$_2$O$_3$ or γ-Fe$_2$O$_3$ at temperatures greater than ∼500 °C, depending on the β-Fe$_2$O$_3$ morphology and annealing conditions.[29] At room temperature pure hematite is a canted antiferromagnet while β-Fe$_2$O$_3$ is paramagnetic. In addition, β-Fe$_2$O$_3$ is reported to possess a bandgap as low as 1.7 eV,[21] suggesting the possibility that it could provide superior solar absorption as compared to α-Fe$_2$O$_3$ and therefore make it a more suitable OER photoanode. This smaller bandgap would also make β-Fe$_2$O$_3$ an outstanding candidate for use in tandem photoelectrochemical cells, for which recent modeling studies predict that an optimized system will require precisely a 1.7 eV bandgap top cell.[30,31] Despite these promising signs, β phase iron oxide has not previously been considered for PEC water splitting applications due to its synthetic elusiveness. We do note, however, that the β phase may have more influence in the study of iron oxide photoanodes than previously thought. For example, Liang et al. have shown that Si-doping of Fe$_2$O$_3$ during spray pyrolysis can have the unintended consequence of partial β-Fe$_2$O$_3$ stabilization, which can be further influenced by choice of substrate.[32] Therefore, considering the current trends of employing dopants (see ref 33. and references therein) and substrate−film interfacial layers[34−38] to improve PEC performance of iron oxide films, a clear understanding of the often unintended consequences (including nonequilibrium phase stabilization) of these treatments is necessary to understand the resultant PEC behavior. Before considering these implications, however, β-Fe$_2$O$_3$ deserves a thorough investigation as a PEC water-splitting material in its own right.

To access the photoelectrochemical properties of β-Fe$_2$O$_3$ we sought a substrate template that is conductive, transparent, and lattice-matched. First, low-index [(001)-, (011)-, and (111)-oriented], double-side polished single crystal YSZ substrates were annealed for 3 h in flowing O$_2$ at 1100 °C to remove polishing damage and achieve atomically flat surfaces. Next, a ∼40 nm thick tin-doped indium oxide (ITO) film was grown by ALD at 225 °C on the YSZ substrates (following the procedures of ref 39) to provide an epitaxial (see Figure S1 in the Supporting Information), transparent, and conducting underlayer template. Heteroepitaxial growth of ITO(001) on YSZ(001) is readily achieved due the small lattice mismatch (∼1%) between YSZ and ITO (0.512 vs 1.012 nm) and similar oxygen sublattices.[40] Finally, a ∼20 nm thick Fe$_2$O$_3$ film was deposited using ferrocene [Fe(Cp)$_2$] and ozone (O$_3$) at 200 °C according to the ALD procedure established in ref 41. A complete description of all growth parameters is included in the Methods section in the Supporting Information. To the best of our knowledge, there is no literature precedence for the epitaxial growth of β-Fe$_2$O$_3$ on any substrate using any deposition technique. However, epitaxial growth is often observed between isomorphic systems with similar material chemistries, even at large (>3%) lattice mismatch.[2] ITO provides an isomorphic substrate with 7% lattice mismatch for growth of β-Fe$_2$O$_3$.

To assess the phase and orientation of ALD-grown Fe$_2$O$_3$ films on ITO/YSZ, we performed conventional X-ray θ-2θ scans and pole figure measurements. Data for the Fe$_2$O$_3$ grown on ITO(001)∥YSZ(001) is shown in Figure 1, whereas data for Fe$_2$O$_3$ on ITO(011)∥YSZ(011) and Fe$_2$O$_3$ on ITO(111)∥YSZ(111) is provided in Figure S2 in the Supporting Information. Figure 1a shows specular thin film diffraction data as a function of out-of-plane momentum transfer, $q_z = 4\pi \sin(2\theta/2)/\lambda$, where 2θ is the scattering angle and λ = 0.752 Å is the X-ray wavelength. The strong peaks are indexed as YSZ(002), ITO(004), and β-Fe$_2$O$_3$(004), respectively, as a function of increasing q_z. Kiessig fringes resolved about the β-Fe$_2$O$_3$(004) reflection attest to the uniformity, smoothness, and well-defined thickness of the β-Fe$_2$O$_3$ film. We note that there is a weak (1/10000 as intense as the ITO(004) reflection) ITO(222) peak at q_z = 2.16 arising from a small minority of misoriented ITO crystallites.

X-ray pole figures for β-Fe$_2$O$_3$ grown on ITO(001)∥YSZ(001) in Figure 1b (data for other orientations are provided in the Supporting Information, Figure S2) are representations of the statistical distribution of the crystallite orientations within a sample, plotted as a function of colatitude angle χ and azimuthal angle φ. The use of synchrotron radiation at the Advanced Photon Source's Sector 33-BM-C and an area detector enabled the simultaneous collection of reflections satisfying Bragg conditions in the |q| range of =2.25−2.35 Å^{-1} (e.g., refs 42−43). This range encompasses only the ITO{123}, β-Fe$_2$O$_3${222}, and α-Fe$_2$O$_3${10$\bar{1}$4} family of reflections. Comparison of the data in Figure 1b with simulated patterns (Figure 1d), derived from a cube-on-cube-on-cube epitaxial relationship (Figure 1c), show excellent agreement, thereby validating the epitaxial model. We note that the pole figure data in Figure 1b does show exceedingly weak Bragg reflections from <1% phase fraction of epitaxial α-Fe$_2$O$_3$ (compare Figure 1b, d). A brief discussion of this trace phase is included in the Supporting Information. Despite the high phase sensitivity of the synchrotron-based measurement, no intensity from α-Fe$_2$O$_3${10$\bar{1}$4} reflections were observable for
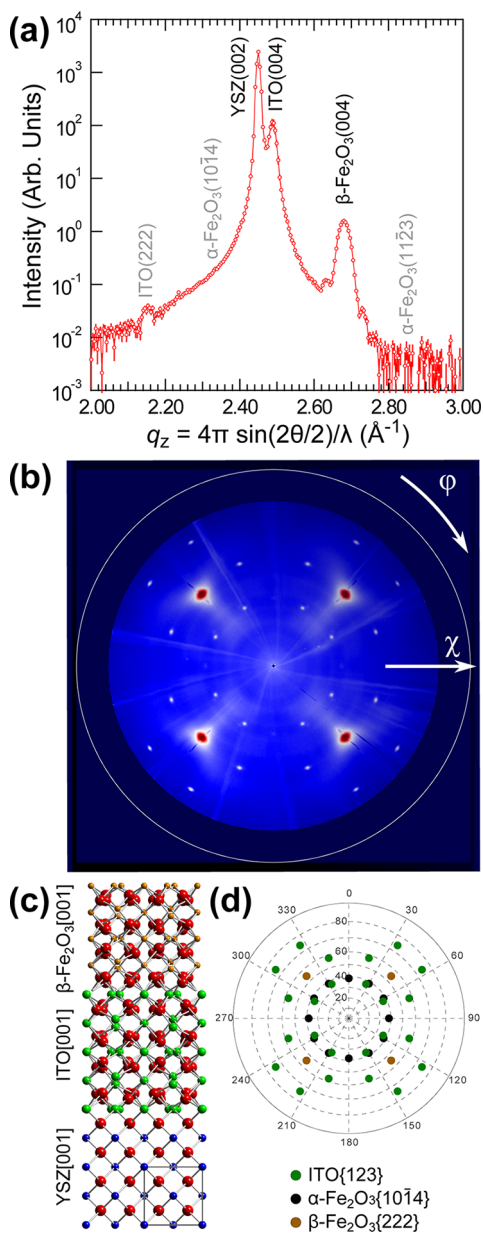
Figure 1. X-ray characterization of β-Fe_2O_3 grown on ITO(001)||YSZ(001). (a) Out-of-plane thin-film X-ray diffraction. Apart from a weak polycrystalline ITO(222) signal, only the reflections from YSZ(002), ITO(004), and β-Fe_2O_3(004) are present, indicating cube-on-cube-on-cube epitaxy. Unobserved α-Fe_2O_3 reflections that would appear within this |q| range are denoted in gray. (b) X-ray pole figure acquired over a |q| range of 2.25–2.35 Å^{-1} encompassing ITO{123}, β-Fe_2O_3{222}, and α-Fe_2O_3{10$\bar{1}$4} families of reflections. Intensity is logarithmically scaled. (c) An idealized cube-on-cube-on-cube heteroepitaxial oxide stack produces simulated pole figures in d, which match well with the measured data in b.

the other low-index systems (see Figure S2 in the Supporting Information), indicating crystalline-phase pure films. Supplementary phase verification from Raman scattering is also provided as Figure S3 in the Supporting Information. Hereafter, we will refer to these epitaxial β phase films by their out-of-plane orientation, e.g. β-Fe_2O_3(001)||ITO(001)||YSZ(001) is simply β-Fe_2O_3(001).

High-resolution cross-sectional transmission electron microscopy (TEM) of the β-Fe_2O_3(001)||ITO(001) boundary
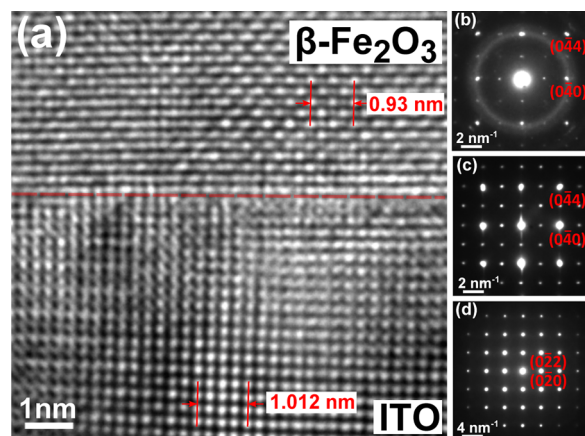

Figure 2. High-resolution cross-sectional TEM results. (a) TEM image showing the β-Fe_2O_3(001)||ITO(001) interface. (b–d) Electron diffraction patterns along the [100] axes of β-Fe_2O_3, ITO, and YSZ, respectively. The rings in b are due to the amorphous platinum layers on top of the β-Fe_2O_3 layer.

provides further insight into the coherency and quality of the heterointerface. Figure 2 shows the TEM image of the β-Fe_2O_3(001)||ITO(001) interface and the electron diffraction patterns of β-Fe_2O_3, ITO, and YSZ, all along the [100] direction. The Fe_2O_3(001)||ITO(001) cube-on-cube epitaxy is clearly revealed in Figure 2a, and the crystallinity of the β-Fe_2O_3 is confirmed by the nanobeam diffraction (Figure 2b). The diffraction also indicates that the epitaxy is preserved throughout the entire β-Fe_2O_3 sample thickness. Interfacial strain due to the large lattice mismatch between β-Fe_2O_3 and ITO (~7%) is mitigated via the formation of misfit dislocations in β-Fe_2O_3 (see Figure S4 in the Supporting Information).

With a clear understanding of the structure and phase of these Fe_2O_3 films, we proceed to optical and PEC characterization. Figure 3a shows reflectance-corrected absorbance spectra for all low-index orientations of β-Fe_2O_3, as well as comparative data for α-Fe_2O_3 on fluorine-doped tin oxide (FTO) and polycrystalline β-Fe_2O_3/ITO on fused quartz (FQ). For β-Fe_2O_3/ITO/FQ phase verification, see Raman data in Figure S3 in the Supporting Information. There is little difference in the absorbance between the three orientations of epitaxial β-Fe_2O_3, but the β-Fe_2O_3/ITO/FQ shows comparatively weaker absorption at shorter wavelengths. This may be attributable to thickness variation between epitaxial and polycrystalline β-Fe_2O_3, but previous reports have found reduced absorption in α-Fe_2O_3 to be correlated with decreased crystallite size and Fe–O_6 octahedral distortion.[44] Compared to α phase samples, the β phase samples lack distinct optical absorption features. Literature reports of absorption spectra for β-Fe_2O_3 agree closely with our observations in Figure 3a.[21,22] However, the presence of some amorphous phase fraction is not inconsistent with the optical properties, nor can it be excluded by the diffraction or Raman data.

Tauc plots ($\alpha h\upsilon^n$ vs $h\upsilon$, where α is the absorption coefficient and $h\upsilon$ is the photon energy) assuming an indirect allowed transition ($n = 1/2$)[22] reveal a bandgap of 1.8 eV for all β phase thin films (Figure 3b). This value is 0.1 eV less than our α-Fe_2O_3 control sample and as much as 0.4 eV smaller than the commonly cited α-Fe_2O_3 bandgap. This smaller β phase bandgap may ultimately prove an advantage compared to that of α-Fe_2O_3 in tandem PEC water splitting cells, as predicted by recent bandgap optimization models.[30,31]
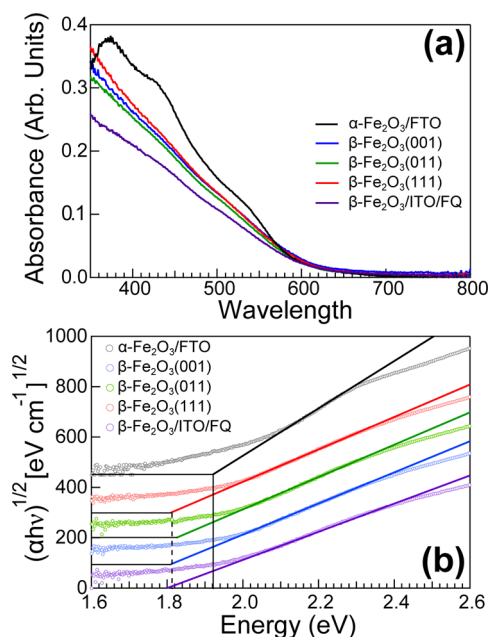
Figure 3. Optical absorbance data for β-Fe$_2$O$_3$ series and α-Fe$_2$O$_3$ control. (a) Reflection-corrected absorbance for epitaxial β phase thin films are nominally identical, while polycrystalline β-Fe$_2$O$_3$/ITO/FQ shows weaker absorption and the α-Fe$_2$O$_3$ control shows more distinct optical transitions. (b) Allowed, indirect bandgap Tauc analysis estimates a consistently lower bandgap for all β phase thin films as compared to the α phase. Tauc plots are offset for clarity.

PEC behavior for the β-Fe$_2$O$_3$ series was assessed by measuring current density (J) as a function of applied voltage (V) in the dark and under AM 1.5 illumination (100 mW cm^{-2}) with a three-electrode setup in 1 M KOH. Results for postannealed α-Fe$_2$O$_3$/FTO are included for comparison (Figure 4a). Upon illumination, the epitaxial β-Fe$_2$O$_3$ samples are photoactive without post-annealing, which is atypical of Fe$_2$O$_3$ films grown by the Fe(Cp)$_2$-O$_3$ ALD process.[45] Photocurrent onset potentials (E_{onset}) differed between the three orientations, shifting cathodically by 0.1 V_{RHE} for both β-Fe$_2$O$_3$(011) and β-Fe$_2$O$_3$(111) as compared to β-Fe$_2$O$_3$(001). These shifts suggest the possibility of a variation in the OER reactivity of the three films because of the differing preferred orientation of the β-Fe$_2$O$_3$ crystallites. These differing preferred orientations may lead to the exposure of different crystal terminations at the semiconductor-electrolyte interface, each with distinct OER activity. Still, the plateau current for all three epitaxial samples is similar at $J \sim 0.3$ mA/cm^2. Chronoamperometry reveals that the plateau photocurrent is stable at 1.53 V vs RHE for all films for at least 1000 s (see Figure S5 in the Supporting Information). We also observe that single crystal YSZ substrates are not required to achieve PEC-active β-Fe$_2$O$_3$ thin films as deposition of Fe$_2$O$_3$ on polycrystalline ITO on fused quartz also results in an as-deposited photoactive β-Fe$_2$O$_3$ film. This sample was the worst performer of the β-phase series, however, conceivably because of a higher density of charge recombination centers that may be found at high-angle grain boundaries in such polycrystalline films.[46]

Further disentanglement of the differences in PEC behavior among the β phase series is possible through utilization of a PEC hole scavenger.[47,48] Use of H$_2$O$_2$ as a hole scavenger circumvents hole capture limitations when assessed in conjunction with J–V measurements employed in conventional
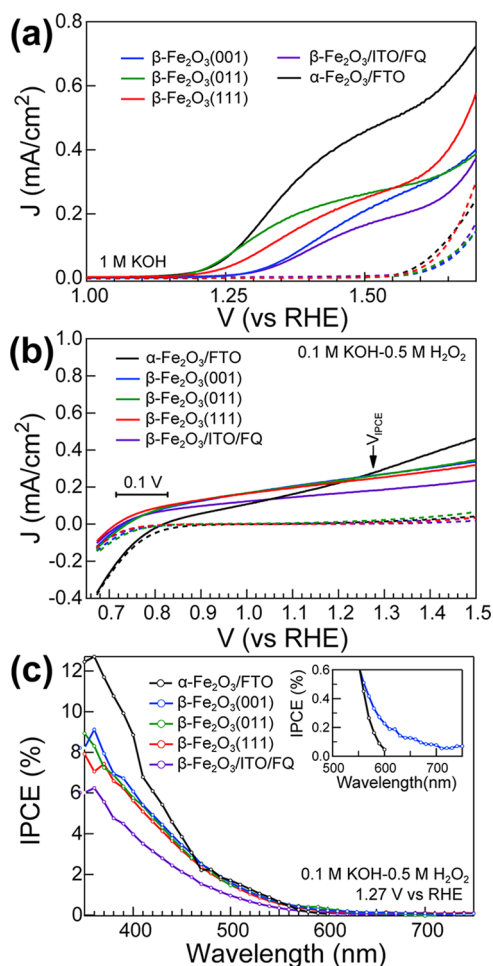
Figure 4. Photoelectrochemical data for low-index β-Fe$_2$O$_3$/ITO/YSZ, β-Fe$_2$O$_3$/ITO/FQ, and α-Fe$_2$O$_3$ photoanodes. (a) J–V measurements in dark (dotted line) and under white light (solid line) in 1 M KOH show photoactive as-deposited β-Fe$_2$O$_3$ films with onset voltages and plateau photocurrent dependent on crystallite orientation. (b) J–V measurements in dark (dotted line) and in light (solid line) in 0.1 M KOH and 0.5 M H$_2$O$_2$ reveal a 0.1 V earlier photocurrent onset for β-Fe$_2$O$_3$ relative to α-Fe$_2$O$_3$. (c) IPCEs for epitaxial β-Fe$_2$O$_3$ films measured at 1.27 vs RHE in 0.1 M KOH and 0.5 M H$_2$O$_2$ are insensitive to thin film orientation and show mildly improved IPCE above 600 nm, as compared to α-Fe$_2$O$_3$ (inset).

KOH electrolyte.[48] We therefore performed J–V measurements in 0.1 M KOH and 0.5 M H$_2$O$_2$ for both the β phase series and the α phase control (Figure 4b). In contrast to the results in Figure 4a, all epitaxial β-Fe$_2$O$_3$ samples exhibited essentially identical J–V behavior, implying the differences observed without H$_2$O$_2$ are dominated by changes in water oxidation (OER) catalytic efficiency at the electrolyte/β-Fe$_2$O$_3$ interface. In addition, the β-Fe$_2$O$_3$/ITO/FQ sample, while exhibiting a similar onset potential to epitaxial β-phase samples, still shows a lower plateau current density. The lower light harvesting efficiency of this polycrystalline film will contribute to lower performance but is not sufficient to fully account for the difference. This further corroborates the possibility that the lower performance of the polycrystalline β-Fe$_2$O$_3$ may be related to its grain structure and resulting bulk recombination states at β-Fe$_2$O$_3$ grain boundaries and/or the β-Fe$_2$O$_3$/ITO interface.

The utilization of the hole scavenger also allows for the OER-independent comparison of α- and β-Fe$_2$O$_3$ PEC performance. In general, the high overpotentials required to activate α-Fe$_2$O$_3$ photoanodes in water are attributed to electron–hole recombination losses in the bulk, depletion, and surface regions of the film. However, as observed by Dotan et al.,[48] the elimination of the hole injection barrier isolates bulk and depletion region contributions in the J–V data. In the presence of H$_2$O$_2$, we find a consistently more cathodic onset potential in all β phase samples by ~0.1 V_{RHE} as compared to the α phase control. This suggests that the β-Fe$_2$O$_3$ either exhibits a significantly lower recombination rate or possesses a negatively shifted flat-band potential relative to α-Fe$_2$O$_3$, thereby reducing the applied potential required for the separation of charge carriers. While the development of a larger built-in photo-voltage has not been excluded, it seems less likely given a smaller bandgap and comparable photon-to-current efficiency (see discussion below). As such, the band alignment of β-Fe$_2$O$_3$ may be inherently better suited to PEC water oxidation relative to α-Fe$_2$O$_3$. However, we note that cathodic shifts in the onset potential have also been achieved in α-Fe$_2$O$_3$ photoanodes by utilizing oxide buffer layers prior to Fe$_2$O$_3$ deposition[36] or electron blocking layers that selectively pass holes to the electrolyte. Regardless, as significant modification of inherent materials properties (bulk recombination rate, band edge alignment) is rare, phase selection strategies such as β-phase stabilization provide an uncommon opportunity to circumvent these limits. While utilization of a hole scavenger in practical applications is unrealistic, the lower onset potential for β-Fe$_2$O$_3$ photocurrent in H$_2$O$_2$ solutions suggests ample room for future improvements by using OER surface catalysts, a route to reducing hole injection barrier without sacrificial reagents.

Incident photon-to-current efficiencies (IPCEs), Figure 4c, were acquired at 1.27 V vs RHE in 0.1 M KOH and 0.5 M H$_2$O$_2$ to minimize the influence of OER surface reaction kinetics and to probe IPCE behavior at comparable current densities. Epitaxial β-Fe$_2$O$_3$ films behave nearly identically. As is consistent with the generally lower photocurrent for poly-crystalline β-Fe$_2$O$_3$ at all applied potentials in the J–V measurements (Figure 4a, b), the β-Fe$_2$O$_3$/ITO/FQ hetero-structures shows consistently lower IPCE across the entire spectrum. All β phase samples have slightly lower IPCEs compared to the α phase in the blue until ~460 nm, at which point (inset) the two phases are indistinguishable before a drop-off in α phase IPCE at 550 nm. α-Fe$_2$O$_3$ IPCE data is at the dark current floor beyond 600 nm, while the β-Fe$_2$O$_3$ samples (Figure 4c inset shows only β-Fe$_2$O$_3$(001) for clarity) have weak, but measurable (0.1%), IPCE in this regime. Although the IPCE of these unoptimized β phase samples above 600 nm is quite low, the extension of photosensitivity into the red part of the solar spectrum is clearly a real advantage of this phase. Stable photocurrent densities recorded under pH 13.1 operation for at least 15 min (see Figure S5 in the Supporting Information) further attest to the potential of β-Fe$_2$O$_3$ in water oxidation applications.

Although there is little work on the influence of epitaxy on Fe$_2$O$_3$ photoanodes for PEC water splitting (for examples, see refs 49–52), those works are tangential to the recent trend in the utilization of oxide underlayers to improve α-Fe$_2$O$_3$ PEC performance. The insights reported herein provide improved understanding of the mechanism by which underlayers influence α-Fe$_2$O$_3$ water oxidation behavior, including crystallographic templating effects or minority phase contributions. We

first cite Zandi et al., who found enhanced PEC behavior for annealed, ultrathin (<18 nm) α-Fe$_2$O$_3$ films on commercial ITO.[38] Because of the similarity between their substrate selection and ours, it is possible that they also stabilized β-Fe$_2$O$_3$ during growth and transformed it to α-Fe$_2$O$_3$ upon annealing at 500 °C (no as-deposited data were presented). The morphology of the β-Fe$_2$O$_3$ may dictate the properties of the resultant α-Fe$_2$O$_3$ film and should be more clearly understood to precisely control its properties. The mechanism for the improved structure afforded by other underlayers is less clear due to their X-ray amorphous nature (for tabulated crystallinity results, see ref 9) at the reported deposition conditions. Still, short and medium range surface atom ordering may significantly influence the crystallinity of the subsequently grown thin films. ALD of Nb$_2$O$_5$ using Nb$_2$(OC$_2$H$_5$)$_{10}$ and H$_2$O is nominally amorphous throughout the ALD window. Growth of TiO$_2$ at 120 °C using tetrakis(dimethylamino)Ti-(IV) and H$_2$O, as reported in ref 37, is also amorphous, as well as WO$_3$ using W$_2$(NMe$_2$)$_6$ and H$_2$O. ALD of Ga$_2$O$_3$ under the quoted growth and annealing conditions of ref 36. was also found to be amorphous.[53] Even if crystallization does occur, a stable monoclinic β-Ga$_2$O$_3$ phase, not corundum-type α-Ga$_2$O$_3$ is expected to develop at ~700 °C. This does not preclude improved crystallinity of α-Fe$_2$O$_3$ when deposited on a Ga$_2$O$_3$ buffer layer, and indeed subsequent analyses revealed sharper and more intense α-Fe$_2$O$_3$ Raman features for similar samples,[38] as is consistent with formation of large, homogeneous crystalline grains. Regardless, any designation of improved crystallinity due to isostructural templating is unlikely in this case as well, and care must be taken when identifying such mechanisms as the source for improved PEC performance.

In conclusion, we have reported the epitaxial stabilization of the uncommon β phase of Fe$_2$O$_3$ using ALD and an isomorphic ITO/YSZ substrate. This isomorphic stabilization also occurs for polycrystalline ITO grown on fused quartz, thereby eliminating the need for a single crystal substrate to obtain the β phase. β-Fe$_2$O$_3$ films are crystalline and photoactive as deposited, properties that are atypical for ALD-grown Fe$_2$O$_3$ films using Fe(Cp)$_2$ and O$_3$. The orientation of β phase crystallites is controlled through selection of the epitaxial ITO/YSZ substrate, which influences PEC activity when measured in 1 M KOH, but not when employing 0.5 M H$_2$O$_2$ as a rapid hole scavenger. This indicates that while the surface-dominated recombination and OER properties of β-Fe$_2$O$_3$ are affected by crystallite orientation, the bulk film properties are not, as may be expected for a highly symmetric crystal system. When measured in 0.5 M H$_2$O$_2$, β-Fe$_2$O$_3$ shows a 0.1 V more cathodic onset potential relative to the α phase. The β phase also shows stable operation in strong base in addition to a slightly enhanced IPCE in the red (>600 nm) portion of the solar spectrum, likely due to a bandgap that is at least 0.1 eV more narrow. The modest improvements in bandgap, photocurrent onset, and red light conversion efficiency for β-Fe$_2$O$_3$ are enhancements that are notoriously difficult to achieve in α-Fe$_2$O$_3$. As this work represents the first PEC water oxidation study of β-Fe$_2$O$_3$, further optimization and assessment will be required to fully assess the potential of this iron(III) oxide phase for PEC solar energy conversion applications.

■ ASSOCIATED CONTENT

Ⓢ Supporting Information

X-ray diffraction data verifying ITO/YSZ epitaxy, specular X-ray scattering, and pole figure measurements for β-Fe$_2$O$_3$(011)

and β-Fe$_2$O$_3$(111), Raman scattering for all samples, additional TEM images, and chronoamperometry data to assess β-Fe$_2$O$_3$ stability at PEC operating conditions. This material is available free of charge via the Internet at http://pubs.acs.org/.

■ AUTHOR INFORMATION

Corresponding Author
*E-mail: martinson@anl.gov.

Notes
The authors declare no competing financial interest.

■ ACKNOWLEDGMENTS

■ REFERENCES

(1) Farrow, R. The Stabilization of Metastable Phases by Epitaxy. *J. Vac. Sci. Technol., B* **1983**, *1*, 222−228.

(2) Gorbenko, O. Y.; Samoilenkov, S. V.; Graboy, I. E.; Kaul, A. R. Epitaxial Stabilization of Oxides in Thin Films. *Chem. Mater.* **2002**, *14*, 4026−4043.

(3) Schlom, D. G.; Chen, L. Q.; Pan, X.; Schmehl, A.; Zurbuchen, M. A. A Thin Film Approach to Engineering Functionality into Oxides. *J. Am. Ceram. Soc.* **2008**, *91*, 2429−2454.

(4) Balasubramaniam, K.; Havelia, S.; Salvador, P.; Zheng, H.; Mitchell, J. Epitaxial stabilization and Structural properties of REMnO$_3$ (RE = Dy, Gd, Sm) Compounds in a Layered, Hexagonal ABO$_3$ Structure. *Appl. Phys. Lett.* **2007**, *91*, 232901.

(5) Xiao, R. F.; Ng, L.; Yu, P.; Wong, G. Preparation of Crystalline Beta Barium Borate (β-BaB$_2$O$_4$) Thin Films by Pulsed Laser Deposition. *Appl. Phys. Lett.* **1995**, *67*, 305−307.

(6) Moreira dos Santos, A. F.; Cheetham, A. K.; Tian, W.; Pan, X.; Jia, Y.; Murphy, N. J.; Lettieri, J.; Schlom, D. G. Epitaxial Growth and Properties of Metastable BiMnO$_3$ Thin Films. *Appl. Phys. Lett.* **2004**, *84*, 91−93.

(7) Leskelä, M.; Ritala, M. Atomic Layer Deposition (ALD): From Precursors to Thin Film Structures. *Thin Solid Films* **2002**, *409*, 138−146.

(8) George, S. M. Atomic Layer Deposition: An Overview. *Chem. Rev.* **2009**, *110*, 111−131.

(9) Miikkulainen, V.; Leskelä, M.; Ritala, M.; Puurunen, R. L. Crystallinity of Inorganic Films Grown by Atomic Layer Deposition: Overview and General Trends. *J. Appl. Phys.* **2013**, *113*, 021301.

(10) Lewis, N. S.; Nocera, D. G. Powering the Planet: Chemical Challenges in Solar Energy Utilization. *Proc. Natl. Acad. Sci. U.S.A.* **2006**, *103*, 15729−15735.

(11) Osterloh, F. E. Inorganic Materials as Catalysts for Photochemical Splitting of Water. *Chem. Mater.* **2007**, *20*, 35−54.

(12) Walter, M. G.; Warren, E. L.; McKone, J. R.; Boettcher, S. W.; Mi, Q.; Santori, E. A.; Lewis, N. S. Solar Water Splitting Cells. *Chem. Rev.* **2010**, *110*, 6446−6473.

(13) Cho, S.; Jang, J.-W.; Lee, K.-H.; Lee, J. S. Research Update: Strategies for Efficient Photoelectrochemical Water Splitting Using Metal Oxide Photoanodes. *APL Mater.* **2014**, *2*, 010703.

(14) Sivula, K.; Le Formal, F.; Grätzel, M. Solar Water Splitting: Progress Using Hematite (α-Fe$_2$O$_3$) Photoelectrodes. *ChemSusChem* **2011**, *4*, 432−449.

(15) Katz, M. J.; Riha, S. C.; Jeong, N. C.; Martinson, A. B.; Farha, O. K.; Hupp, J. T. Toward Solar Fuels: Water Splitting with Sunlight and "Rust"? *Coord. Chem. Rev.* **2012**, *256*, 2521−2529.

(16) Kim, J. Y.; Magesh, G.; Youn, D. H.; Jang, J.-W.; Kubota, J.; Domen, K.; Lee, J. S. Single-Crystalline, Wormlike Hematite Photoanodes for Efficient Solar Water Splitting. *Sci. Rep* **2013**, *3*, 2631.

(17) Svendsen, M. B. Beta-Fe$_2$O$_3$- Eine Neue Eisen (III) Oxyd-Struktur. *Naturwissenschaften* **1958**, *45*, 542−542.

(18) Ikeda, Y.; Takano, M.; Bando, Y. Formation Mechanism of Needle-like α-Fe$_2$O$_3$ Particles Grown Along the c-Axis and Characterization of Precursorily Formed β-Fe$_2$O$_3$. *Bull. Inst. Chem. Res., Kyoto Univ.* **1986**, *64*, 249−258.

(19) Danno, T.; Nakatsuka, D.; Kusano, Y.; Asaoka, H.; Nakanishi, M.; Fujii, T.; Ikeda, Y.; Takada, J. Crystal Structure of β-Fe$_2$O$_3$ and Topotactic Phase Transformation to α-Fe$_2$O$_3$. *Cryst. Growth Des.* **2013**, *13*, 770−774.

(20) Sakurai, S.; Namai, A.; Hashimoto, K.; Ohkoshi, S.-i. First Observation of Phase Transformation of All Four Fe$_2$O$_3$ Phases ($\gamma \rightarrow \varepsilon \rightarrow \beta \rightarrow \alpha$-Phase). *J. Am. Chem. Soc.* **2009**, *131*, 18299−18303.

(21) Ben-Dor, L.; Fischbein, E.; Felner, I.; Kalman, Z. β-Fe$_2$O$_3$: Preparation of Thin Films by Chemical Vapor Deposition from Organometallic Chelates and Their Characterization. *J. Electrochem. Soc.* **1977**, *124*, 451−457.

(22) Barreca, D.; Carraro, G.; Devi, A.; Fois, E.; Gasparotto, A.; Seraglia, R.; Maccato, C.; Sada, C.; Tabacchi, G.; Tondello, E. β-Fe$_2$O$_3$ Nanomaterials from an Iron (II) Diketonate-Diamine Complex: A Study from Molecular Precursor to Growth Process. *Dalton Trans.* **2012**, *41*, 149−155.

(23) Kuribayashi, K.; Ueyama, R. Effect of the Substrate on the Growth of Spinel Iron Oxide Thin Films by Metal-Organic Chemical Vapor Deposition. *Thin Solid Films* **1997**, *295*, 16−18.

(24) Maruyama, T.; Kanagawa, T. Electrochromic Properties of Iron Oxide Thin Films Prepared by Chemical Vapor Deposition. *J. Electrochem. Soc.* **1996**, *143*, 1675−1677.

(25) Zboril, R.; Mashlan, M.; Barcova, K.; Vujtek, M. Thermally Induced Solid-State Syntheses of γ-Fe$_2$O$_3$ Nanoparticles and Their Transformation to α-Fe$_2$O$_3$ via ε-Fe$_2$O$_3$. *Hyperfine Interact.* **2002**, *139*, 597−606.

(26) Rahman, M. M.; Jamal, A.; Khan, S. B. Faisal, M. Characterization and Applications of As-Grown β-Fe$_2$O$_3$ Nanoparticles Prepared by Hydrothermal Method. *J. Nanopart. Res.* **2011**, *13*, 3789−3799.

(27) Carraro, G.; Barreca, D.; Comini, E.; Gasparotto, A.; Maccato, C.; Sada, C.; Sberveglieri, G. Controlled Synthesis and Properties of β-Fe$_2$O$_3$ Nanosystems Functionalized with Ag or Pt Nanoparticles. *CrystEngComm* **2012**, *14*, 6469−6476.

(28) Carraro, G.; Maccato, C.; Gasparotto, A.; Montini, T.; Turner, S.; Lebedev, O. I.; Gombac, V.; Adami, G.; Van Tendeloo, G.; Barreca, D. Enhanced Hydrogen Production by Photoreforming of Renewable Oxygenates Through Nanostructured Fe$_2$O$_3$ Polymorphs. *Adv. Funct. Mater.* **2014**, *24*, 372−378.

(29) Zboril, R.; Mashlan, M.; Petridis, D. Iron (III) Oxides from Thermal Processes Synthesis, Structural and Magnetic Properties, Mössbauer Spectroscopy Characterization, and Applications. *Chem. Mater.* **2002**, *14*, 969−982.

(30) Hu, S.; Xiang, C.; Haussener, S.; Berger, A. D.; Lewis, N. S. An Analysis of the Optimal Band Gaps of Light Absorbers in Integrated Tandem Photoelectrochemical Water-Splitting Systems. *Energy Environ. Sci.* **2013**, *6*, 2984−2993.

(31) Seger, B.; Castelli, I. E.; Vesborg, P. C. K.; Jacobsen, K. W.; Hansen, O.; Chorkendorff, I. 2-Photon Tandem Device for Water Splitting: Comparing Photocathode First *Versus* Photoanode First Designs. *Energy Environ. Sci.* **2014**, *7*, 2397−2413.

(32) Liang, Y.; van de Krol, R. Influence of Si Dopant and SnO_2 Interfacial Layer on the Structure of the Spray-Deposited Fe_2O_3 Films. *Chem. Phys. Lett.* **2009**, *479*, 86−90.

(33) Li, Z.; Luo, W.; Zhang, M.; Feng, J.; Zou, Z. Photo-electrochemical Cells for Solar Hydrogen Production: Current State of Promising Photoelectrodes, Methods to Improve Their Properties, and Outlook. *Energy Environ. Sci.* **2013**, *6*, 347−370.

(34) Liang, Y.; Enache, C. S.; van de Krol, R. Photoelectrochemical Characterization of Sprayed α-Fe_2O_3 Thin Films: Influence of Si Doping and SnO_2 Interfacial Layer. *Int. J. Photoenergy* **2008**, *2008*.

(35) Le Formal, F.; Graetzel, M.; Sivula, K. Controlling Photoactivity in Ultrathin Hematite Films for Solar Water-Splitting. *Adv. Funct. Mater.* **2010**, *20*, 1099−1107.

(36) Hisatomi, T.; Brillet, J.; Cornuz, M.; Le Formal, F.; Tétreault, N.; Sivula, K.; Grätzel, M. A Ga_2O_3 Underlayer as an Isomorphic Template for Ultrathin Hematite Films Toward Efficient Photo-electrochemical Water Splitting. *Faraday Discuss.* **2012**, *155*, 223−232.

(37) Hisatomi, T.; Dotan, H.; Stefik, M.; Sivula, K.; Rothschild, A.; Grätzel, M.; Mathews, N. Enhancement in the Performance of Ultrathin Hematite Photoanode for Water Splitting by an Oxide Underlayer. *Adv. Mater.* **2012**, *24*, 2699−2702.

(38) Zandi, O.; Beardslee, J. A.; Hamann, T. Substrate Dependent Water Splitting with Ultrathin α-Fe_2O_3 Electrodes. *J. Phys. Chem. C* **2014**, *118*, 16494−16503.

(39) Elam, J. W.; Baker, D. A.; Martinson, A. B.; Pellin, M. J.; Hupp, J. T. Atomic Layer Deposition of Indium Tin Oxide Thin Films Using Nonhalogenated Precursors. *J. Phys. Chem. C* **2008**, *112*, 1938−1945.

(40) Wong, F. J.; Ramanathan, S. Nonisostructural Complex Oxide Heteroepitaxy. *J. Vac. Sci. Technol. A* **2014**, *32*, -.

(41) Martinson, A. B.; DeVries, M. J.; Libera, J. A.; Christensen, S. T.; Hupp, J. T.; Pellin, M. J.; Elam, J. W. Atomic Layer Deposition of Fe_2O_3 Using Ferrocene and Ozone. *J. Phys. Chem. C* **2011**, *115*, 4333−4339.

(42) Gaudet, S.; De Keyser, K.; Lambert-Milot, S.; Jordan-Sweet, J.; Detavernier, C.; Lavoie, C.; Desjardins, P. Three Dimensional Reciprocal Space Measurement by X-ray Diffraction Using Linear and Area Detectors: Applications to Texture and Defects Determination in Oriented Thin Films and Nanoprecipitates. *J. Vac. Sci. Technol., A* **2013**, *31*, 021505.

(43) Mocuta, C.; Richard, M.-I.; Fouet, J.; Stanescu, S.; Barbier, A.; Guichet, C.; Thomas, O.; Hustache, S.; Zozulya, A. V.; Thiaudiere, D. Fast Pole Figure Acquisition Using Area Detectors at the DiffAbs Beamline-Synchrotron SOLEIL. *J. Appl. Crystallogr.* **2013**, *46*, 1842−1853.

(44) Pailhé, N.; Wattiaux, A.; Gaudon, M.; Demourgues, A. Impact of Structural Features on Pigment Properties of α-Fe_2O_3 Haematite. *J. Solid State Chem.* **2008**, *181*, 2697−2704.

(45) Klahr, B. M.; Martinson, A. B.; Hamann, T. W. Photo-electrochemical Investigation of Ultrathin Film Iron Oxide Solar Cells Prepared by Atomic Layer Deposition. *Langmuir* **2010**, *27*, 461−468.

(46) Warren, S. C.; Voïtchovsky, K.; Dotan, H.; Leroy, C. M.; Cornuz, M.; Stellacci, F.; Hébert, C.; Rothschild, A.; Grätzel, M. Identifying Champion Nanostructures for Solar Water-Splitting. *Nat. Mater.* **2013**, *12*, 842−849.

(47) Iwanski, P.; Curran, J.; Gissler, W.; Memming, R. The Photoelectrochemical Behavior of Ferric Oxide in the Presence of Redox Reagents. *J. Electrochem. Soc.* **1981**, *128*, 2128−2133.

(48) Dotan, H.; Sivula, K.; Grätzel, M.; Rothschild, A.; Warren, S. C. Probing the Photoelectrochemical Properties of Hematite (α-Fe_2O_3) Electrodes Using Hydrogen Peroxide as a Hole Scavenger. *Energy Environ. Sci.* **2011**, *4*, 958−964.

(49) Magnan, H.; Stanescu, D.; Rioult, M.; Fonda, E.; Barbier, A. Enhanced Photoanode Properties of Epitaxial Ti Doped α-Fe_2O_3(0001) Thin Films. *Appl. Phys. Lett.* **2012**, *101*, 133908.

(50) Rioult, M.; Magnan, H.; Stanescu, D.; Barbier, A. Single Crystalline Hematite Films for Solar Water Splitting: Ti-Doping and Thickness Effects. *J. Phys. Chem. C* **2014**, *118*, 3007−3014.

(51) Joly, A. G.; Williams, J. R.; Chambers, S. A.; Xiong, G.; Hess, W. P.; Laman, D. M. Carrier Dynamics in α-Fe_2O_3(0001) Thin Films and Single Crystals Probed by Femtosecond Transient Absorption and Reflectivity. *J. Appl. Phys.* **2006**, *99*, 053521.

(52) Lin, Y.; Zhou, S.; Sheehan, S. W.; Wang, D. Nanonet-Based Hematite Heteronanostructures for Efficient Solar Water Splitting. *J. Am. Chem. Soc.* **2011**, *133*, 2398−2401.

(53) Charles, L., IV; Dezelah, I.; Niinistö, J.; Arstila, K.; Niinistö, L.; Winter, C. H. Atomic Layer Deposition of Ga_2O_3 Films from a Dialkylamido-Based Precursor. *Chem. Mater.* **2006**, *18*, 471−475.